Journal of Materials Chemistry A

ROYAL SOCIETY OF CHEMISTRY

PAPER

View Article Online
View Journal | View Issue

Cite this: J. Mater. Chem. A, 2024, 12, 19137

Acetylacetone functionalized periodic mesoporous organosilicas: from sensing to catalysis†

Chunhui Liu, [abc] Mahdieh Haghighat,[a] Himanshu Sekhar Jena, [a] Dirk Poelman, [b] Nathalie De Geyter, [d] Rino Morent,[d] Anna M. Kaczmarek [*c] and Pascal Van Der Voort [*a]

Received 19th February 2024
Accepted 2nd July 2024

DOI: 10.1039/d4ta01143k

rsc.li/materials-a

25 years after the first papers on the development of Periodic Mesoporous Organosilicas, and in this special issue in honor of prof. Ozin who stood at the cradle of PMOs, we here report for the first time an "acac-PMO" with the acac-functionality intact and embedded in the organic environment of the linker. Periodic mesoporous organosilicas (PMOs) have emerged as versatile sensors due to their stability, low toxicity, and scalability. This study reports for the first time on embedding the acetylacetone (acac) group into the PMO backbone. This integration of acac into the PMO framework opens new applications in both sensing and catalysis. The Eu^{3+} grafted acac-PMOs demonstrate enhanced sensitivity, with a detection limit of 108 nM, and high selectivity in aqueous copper (Cu^{2+}) ion sensing. Additionally, these novel PMOs show high catalytic efficiency in Mannich reactions.

1 Introduction

Periodic mesoporous organosilicas (PMOs) have emerged as a promising and appealing sensor system due to their stable physicochemical properties, low toxicity, high biocompatibility, and facile scalability for large-scale production.[1] PMOs were initially reported in 1999 by Ozin,[2] Stein,[3] and Inagaki.[4] Unlike other porous materials such as MCM (Mobil Composition of Matter)[5] and SBA (Santa Barbara Amorphous materials),[6] PMOs offer the unique advantage of incorporating desired organic functionalities directly into the silsesquioxane framework. This is achieved by utilizing organically bridged silica precursors, where hydrolysable groups (OR) in the bis-silane $(RO)_3$-Si-R_f-Si-$(RO)_3$ are connected to the desired organic functionalities (R_f). The incorporation of these organic groups within the PMO structure enhances the material's hydrophobicity and hydrothermal stability, while also minimizing leaching issues commonly associated with externally grafted functionalities.[7,8] Additionally, PMOs possess ordered mesopores and high surface areas (up to 2370 $m^2\ g^{-1}$),[9] making them suitable for a wide range of applications such as catalysis, adsorption, chromatography, low-k materials, drug release, and sensors.[10–13] The tailored organic functionalities within the PMO framework enable the design of materials with specific properties and functionalities, allowing for enhanced performance in various applications. The ability to finely tune the pore size, surface chemistry, and hydrophobicity of PMOs provides versatility and control over their performance in different environments.

Acetylacetone (acac) based homogeneous transition metal complexes have demonstrated exceptional catalytic efficacy across a variety of organic transformations.[14–16] Significantly, a limited number of acetylacetone-functionalized heterogeneous systems, such as silicas and covalent triazine frameworks (CTFs), have demonstrated high reactivity and recyclability after grafting transition metals (post-synthetic functionalization) in various chemical processes. These processes include cross-coupling reactions, hydroxylation, click chemistry, Glaser-type coupling, and the oxidation of alcohols.[17–22] The immobilization of acac ligands within the framework not only enhances catalytic activity but also provides a stable and recyclable catalytic system, thereby addressing the challenges associated with traditional acac complexes.[17] So far, a PMO with acac functionalities embedded in the backbone has not been reported. Zhao *et al.* grafted the $VO(acac)_2$ onto PMOs to create a catalyst for selective hydroxylation of benzene to phenol.[20] The organic precursor was synthesized through the Schiff base condensation between the amino group of 3-aminopropyl-triethoxysilane (APTES) and the carbonyl unit of $VO(acac)_2$. We aimed to functionalize acac group into a PMO backbone in order to design a robust acac-PMO supported transition metal catalyst for sustainable catalysis.

[a]COMOC – Center for Ordered Materials Organometallics and Catalysis, Department of Chemistry, Ghent University, Krijgslaan 281 S3, 9000 Ghent, Belgium. E-mail: Pascal.VanDerVoort@UGent.be

[b]Lumilab, Department of Solid State Sciences, Ghent University, Krijgslaan 281 S1, 9000 Ghent, Belgium

[c]NanoSensing Group, Department of Chemistry, Ghent University, Krijgslaan 281 S3, 9000 Ghent, Belgium. E-mail: Anna.Kaczmarek@UGent.be

[d]RUPT – Research Unit Plasma Technology, Department of Applied Physics, Ghent University, St-Pietersnieuwstraat 41 B4, 9000 Ghent, Belgium

† Electronic supplementary information (ESI) available. See DOI: https://doi.org/10.1039/d4ta01143k

Next to catalysis where the acac groups are typically tethering transition metal ions, also lanthanides anchor firmly to the acac ligands, creating possibly luminescent sensors. Embedded organic groups within the PMO framework act as efficient energy transfer antennas, sensitizing trivalent lanthanide ions (Ln^{3+}) and promoting luminescence.[13,23,24] The potential applications of such sensors span environmental monitoring, biological analysis, and other areas demanding accurate metal ion detection.[25] Despite this potential, research on lanthanide-based PMOs (LnPMOs) as chemical sensors remains limited, with only a few studies published in the late 2010s.[24,26–30] Among these, Eu-based materials have attracted significant attention for their potential in detecting copper ions (Cu^{2+}).[31–34] Eu-based materials exhibit strong initial fluorescence that undergoes significant quenching upon interaction with Cu ions, offering a highly sensitive and selective detection method for Cu in aqueous solutions.[31,35]

This paper is the first paper that develops an acac-based PMO with embedded acac groups. PMOs are typically made with short rigid bridges for stiffness and extra functionalities on these organic bridges renders the synthesis much more difficult, due to additional interactions with the silane and the surfactant. So, the synthesis of PMOs with such a bulky organic bridge and the acac functionality has produced a material that has high potential.

Acac complexes are generally appreciated because the acac group can tether (hard) transition metals very effectively, this makes them interesting for metal-ion sequestration, water purification, but also for heterogeneous transition metal based catalysis as the metals do not leach from acac groups. But acac groups are also often used in lanthanide (luminescence) chemistry because of the strong interaction and a strong antenna effect. In the past, acac groups have been grafted on oxide materials, such as silica, but the hydrolytic unstable Si–O–Si (siloxane) bond between the silica and the acac containing silane renders these materials less useful in aqueous environments and leaching occurs. This acac-PMO is completely different, the acac groups are covalently bonded to the phenyl rings of the organic bridge, rendering also the local environment more hydrophobic.

Out of a multitude of possible applications for these materials, we have chosen a sensing application and a heterogeneous catalysis application, showcasing that these materials can be used in these applications.

2 Experimental

2.1 Materials and instrumentation

All chemicals were purchased from Sigma Aldrich, Fluorochem, Alfa Aesar, or TCI Europe and used without further purification.

Nitrogen adsorption experiments were conducted at −196 °C using a TriStar II gas analyzer. Prior to analysis, the samples underwent vacuum degassing at 120 °C for 24 h. Powder X-ray diffraction (PXRD) patterns were obtained using a Bruker D8 Advance diffractometer equipped with an autochanger and LynxEye XE-T Silicon Strip Line detector, operating at 40 kV and 30 mA with Cu-Kα radiation ($\lambda = 1.5406$ Å) in Bragg–Brentano geometry. Fourier transform infrared spectroscopy (FT-IR) measurements were performed using a Thermo Nicolet 6700 FT-IR spectrometer equipped with a nitrogen-cooled MCT-A (mercury–cadmium–tellurium) detector and a KBr beam splitter. X-ray fluorescence (XRF) was measured by XRF Supermini200 Rigaku to analyze the relative metal contents. Transmission electron microscopy (TEM) images were acquired using a JEOL JEM-2200FS transmission electron microscope with a post-sample Cs corrector and an accelerating voltage of 200 kV. Using V_2O_5 as a catalyst, elemental analysis (CHNS) was finished using the Thermo Flash 2000 elemental analyzer. X-ray photoelectron spectroscopy (XPS) measurements were carried out on a PHI 5000 VersaProbe II spectrometer equipped with a monochromatic Al-Kα X-ray source ($h\nu = 1486.6$ eV). Photoluminescence measurements were conducted using an Edinburgh Instruments FLSP920 UV-vis-NIR spectrometer setup. The emission signals were detected using a Hamamatsu R928P photomultiplier tube, and a monochromated 450 W xenon lamp was employed as the steady-state excitation source.

2.2 Synthesis

2.2.1 1,3-Bis(4-bromophenyl)propane-1,3-dione (acac-Br). acac-Br was synthesized according to a previously reported procedure.[17] A total of 1.66 g (41.51 mmol) of NaH (60% in mineral oil) was dispersed in 50 mL of anhydrous tetrahydrofuran (THF) under an argon atmosphere and stirred for 30 minutes. The resulting heterogeneous mixture was then transferred to an ice bath, and 2.73 g (13.7 mmol) of solid 4′-bromoacetophenone was added. Once the mixture turned dark red, a solution of methyl 4-bromobenzoate (3.23 g, 15.03 mmol) in anhydrous THF (10 mL) was added dropwise over 30 minutes under an argon atmosphere. The entire mixture was stirred for 1 hour in the ice bath and then for an additional 1 hour at room temperature. The mixture was refluxed for 24 hours under an argon atmosphere, and then quenched with ice. The pH of the reaction mixture was adjusted to neutral by slowly adding 1 N HCl, and the linker was recovered by filtration and washed with distilled H_2O. The resulting sticky dark brown solids were washed with hot ethanol multiple times to obtain the pure linker as a brown solid. Yield: 86%; ^{1}H NMR (400 MHz, DMSO-d_6) δ 8.14–8.09 (m, 4H), 7.81–7.76 (m, 4H), 7.38 (s, 1H). ^{13}C NMR (126 MHz, DMSO-d_6) δ 179.27, 132.10, 126.91, 124.62, 122.13, 89.13. FT-IR spectrum is shown in Fig. S1.†

2.2.2 1,3-Bis(4-((*E*)-2-(triethoxysilyl)vinyl)phenyl)propane-1,3-dione (acac-Si). acac-Si was synthesized *via* a coupling reaction between acac-Br and vinyl-triethoxysilane using Heck reaction conditions. In a two-necked flask under argon, acac-Br (1 g, 2.6 mmol), palladium acetate (5.61 mg, 0.025 mmol), and P(*o*-$CH_3C_6H_4)_3$ (45.7 mg, 0.15 mmol) were combined with freshly distilled DMF (50 mL), triethylamine (2.2 mL, 15.75 mmol), and triethoxyvinylsilane (1.3 mL, 6.25 mmol). The resulting mixture was heated to 100 °C and stirred for 18 hours. After cooling to room temperature and filtration, the solvents were removed, and the remaining heterogeneous residue was dissolved in diethyl ether. Filtration and solvent evaporation yielded the product as a highly viscous orange oil. Yield: 95%;

^{1}H NMR (400 MHz, DMSO-d_6) δ 8.23–8.17 (m, 4H), 7.79–7.74 (m, 4H), 7.22 (d, J = 19.3 Hz, 2H), 6.52–6.43 (m, 2H), 3.83 (q, J = 7.0 Hz, 12H), 3.79 (s, 1H), 1.25–1.12 (m, 18H). ^{13}C NMR (126 MHz, DMSO-d_6) δ 166.55, 136.77, 131.64, 131.24, 129.67, 126.82, 93.43, 57.83, 18.08. FT-IR spectrum is shown in Fig. S1.†

2.2.3 Synthesis of mesoporous acetylacetone-PMO (acac-PMO). Following a modified literature procedure,[36] the synthesis of acac-Si involved a two-step sol–gel reaction. In a 20 mL round bottom flask, cetyl trimethyl-ammonium bromide (CTAB, 0.96 mmol, 350 mg) was dissolved in a solution containing 5.83 g of water. After adding 3.63 mL of NH_4OH solution (25%), the mixture was stirred at 80 °C for 30 minutes. In a separate vial, acac-Si was mixed with bis(triethoxysilyl) ethane (BTESE) in two 0 : 100% and 20 : 80% ratios, respectively, along with 1 mL of ethanol. The precursor solution was then injected promptly into the stirred aqueous surfactant solution, resulting in the formation of a yellow suspension. The mixture was stirred for an additional 24 h at 80 °C. After cooling down and filtration, the solid material was rinsed repeatedly with deionized water and ethanol, followed by drying at 120 °C. To remove the surfactant, a solvent-extraction method was employed with the following procedure: approximately 1 g of the synthesized material was stirred in a solution of 200 mL of ethanol and 3 mL of concentrated hydrochloric acid at 80 °C for 4 hours. This extraction process was repeated twice to ensure the complete removal of all surfactants from the material. Finally, the sample was dried overnight in an oven at 120 °C. The obtained products were denoted as acac(20)-PMO and acac(100)-PMO, for which the molar ratio of acac-Si to BTESE were 20 : 80 and 0 : 100, respectively.

2.2.4 Synthesis of the Eu(III) complex [Eu(tta)$_3$(H$_2$O)$_2$]. Eu(tta)$_3$(H$_2$O)$_2$ was synthesized according to a previously reported procedure.[37] 2-Thenoyltrifluoroacetone (tta, 1.33 g, 6 mmol) was dissolved in 30 mL of ethanol. Sequentially, NaOH (1 N, 6 mL) and a solution of $EuCl_3$ 6H_2O (0.73 g, 2 mmol) in 10 mL of water were added to the 2-thenoyltrifluoroacetone solution. Additional water (200 mL) was added, and the mixture was heated to 60 °C for a brief duration. Upon cooling to room temperature, the complex precipitated. The precipitate was separated by filtration, washed with water, and subsequently dried under vacuum. The yield was 85%, and the complex was found to be a dihydrate. Elemental analysis: calculated for $Eu_1O_6C_{24}H_{12}F_9S_3$: C, 35.35%; H, 1.48%; S, 11.80%. Found C, 34.24%; H, 1.31%; S, 11.57%. IR (KBr, cm^{-1}): 1608 (C=O stretch).

2.2.5 Synthesis of Eu grafted acetylacetone-PMO (acac-PMO@Eu_tta). The materials were synthesized in Pyrex test tubes using a heating block. To 20 mg of the acac(20)-PMO, a 10 times molar amount of the pre-synthesized Eu(tta)$_3$ complex was added. The suspension was subjected to ultrasound for 15 minutes after adding 10 mL of methanol. The Pyrex tubes were then carefully sealed and placed on a heating block at 80 °C for 24 hours. Afterward, the product was allowed to cool to ambient temperature, followed by centrifugation (6000 rpm, 4 min) and two washes with methanol. Finally, the material was dried overnight in an oven at 80 °C.

2.2.6 Synthesis of V grafted acetylacetone-PMO (acac-PMO@VO_acac). The acac-PMO@VO_acac catalyst was prepared using the postsynthetic metalation method, with VO(acac)$_2$ as the metal source and toluene as the solvent. In a typical procedure,[17] 30 mg (0.11 mmol) of VO(acac)$_2$ was dissolved in 15 mL of anhydrous toluene, and 120 mg of acac(100)-PMO was added to the solution under argon atmosphere. The mixture was refluxed overnight with stirring, then filtered and dried. To remove weakly bound VO(acac)$_2$, the catalyst was thoroughly washed using Soxhlet extraction with toluene, followed by filtration and further drying under vacuum. Finally, the catalyst was subjected to vacuum drying at 120 °C for 12 hours to remove any remaining solvent before being used for subsequent experiments. Elemental analysis: C, 55.321; H, 3.818 (acac(100)-PMO); C, 43.18%; H, 4.33% (acac(100)-PMO@VO_acac). V loading (0.59 mmol g^{-1}) was studied by XRF on a Rigaku NEX CG with an Al source and the Al-Kα peak energy was used as the internal standard.

2.2.7 Luminescence-sensing experiment. 1 mg of acac(20)-PMO@Eu_tta was dispersed in 1 mL of M(NO$_3$)$_z$ (1000 ppm) aqueous solutions (M^{z+} = Pb^{2+}, Na^+, Al^{3+}, K^+, Mg^{2+}, Ca^{2+}, Sr^{2+}, Fe^{3+}, Hg^{2+}, Cr^{3+}, Y^{3+}, Zn^{2+}, and Cu^{2+}) at room temperature. The mixture was sonicated for 10 minutes to incorporate metal cations. The suspensions are used for luminescence measurements.

2.2.8 Catalytic tests. During a typical catalytic test, predetermined quantities of 2-naphthol (0.17 mmol) and *N*-methylmorpholine *N*-oxide (NMO) (0.34 mmol), along with the catalyst were combined. The mixture was then refluxed in anhydrous DCM (5 mL) within a 10 mL Schlenk tube under an inert atmosphere. At specific time intervals, the catalyst was separated using syringe filter, and the filtrate was evaporated until dryness, resulting in the formation of the pure Mannich base with a quantitative yield, confirmed by ^{1}H NMR analysis.

3 Results and discussion

3.1 Synthesis and characterization of acac-PMOs

The designed approach for producing specific acac-PMO materials is shown in Scheme 1. This method encompasses an initial base-catalysed condensation between 4′-bromoacetophenone and methyl 4-bromobenzoate.[38] Subsequently, a coupling reaction is performed, involving vinyl-triethoxysilane and using Heck reaction conditions. Through the silylation of acac-Br, the resultant structure of acac-Si is achieved. To create a series of acac-functionalized PMO materials with varying precursor ratios, a combination of acac-Si and bis(triethoxysilyl) ethane (BTESE) is prepared in two distinct ratios: 20% acac-Si to 80% BTESE, and 100% acac-Si to 0% BTESE. The generated products are designated as acac(20)-PMO and acac(100)-PMO, wherein the molar ratios of acac-Si to BTESE are 20 : 80 and 100 : 0, respectively. In the design of acac(20)-PMO@Eu_acac for copper ion sensing, a 20% acetylacetonate (acac) functionalization is strategically chosen to address aggregation-caused quenching (ACQ). This lower acac content ensures an optimal dispersion of Eu^{3+} complexes within the mesoporous framework, maintaining their luminescent efficiency vital for

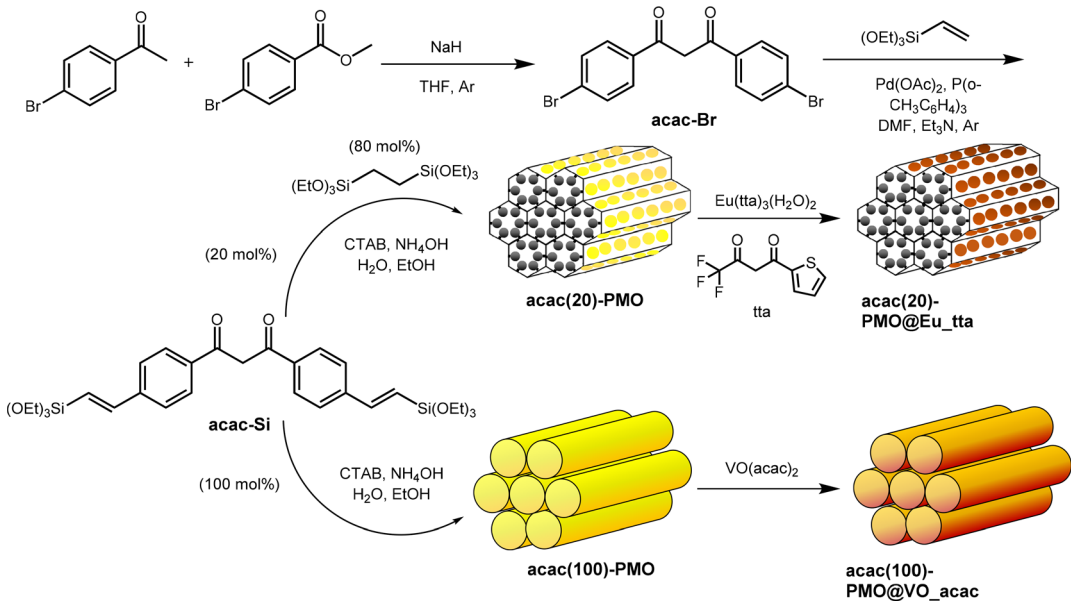

Scheme 1 Schematic illustration of the preparation of the acac(20)-PMO@Eu_tta, acac(100)-PMO@VO_acac.

sensitive and accurate copper detection. The tailored PMO structure facilitates effective interaction with copper ions while preserving the unique luminescent properties of Eu, overcoming the common challenge of luminescence quenching in aggregated lanthanide materials.[39]

The successful coupling was validated through FT-IR measurements. In Fig. 1a and d, we present a spectral analysis comparing the spectrum of pure acac(100)-PMO with that of acac(20)-PMO, as well as their respective metal-grafted counterparts. In the spectra of acac(20)-PMO and acac(100)-PMO, in addition to observing the characteristic C–H and Si–O–Si stretching vibrations at 2950–2800 cm^{-1}, 1200–1000 cm^{-1}, and 800 cm^{-1}, a distinct and sharp band at 1700 cm^{-1} (–C=O) was detected in both acac(20)-PMO and acac(100)-PMO.[17,40] This observation provides clear evidence of the persistence of the acac functional group even after the synthesis of PMO.

To investigate the impact of material functionalization on structural characteristics, we conducted powder X-ray diffraction (PXRD) and N_2-sorption analyses. Fig. 1b displays the X-ray diffraction (XRD) pattern of the acac(20)-PMO within the 2θ

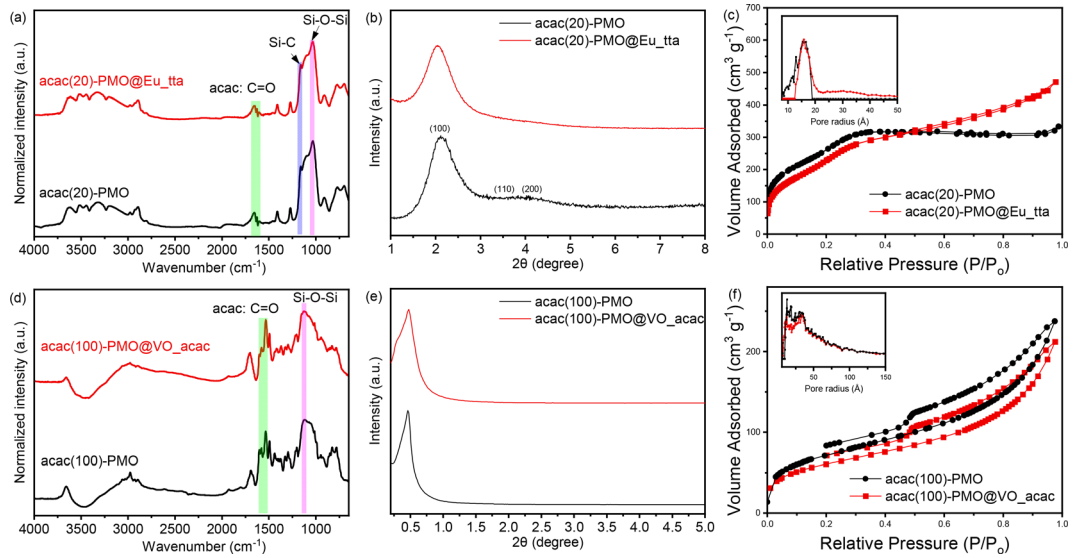

Fig. 1 FT-IR spectra of (a) acac(20)-PMO and (d) acac(100)-PMO; XRD patterns of (b) acac(20)-PMO and (e) acac(100)-PMO; N_2 adsorption–desorption isotherms and pore size distributions of (c) acac(20)-PMO and (f) acac(100)-PMO.

Table 1 Physicochemical properties of samples

Sample	S_{BET} ($m^2\ g^{-1}$)	V ($cm^3\ g^{-1}$)	d_{NLDFT}[a] (nm)
acac(20)-PMO	1040	0.47	3.2
acac(20)-PMO@Eu_tta	984	0.46	3.2
acac(100)-PMO	264	0.36	2.6
acac(100)-PMO@VO_acac	220	0.32	2.6

[a] Calculated from NLDFT, N_2 at 77 K, using the kernel of silica cylindrical pore, adsorption branch.

range of 1–8°. An intense peak at around 2° with a small shoulder was observed in Fig. 1b, signifying the presence of hexagonally (or cubic) arranged mesoporous structures.[41,42] The XRD pattern of acac(100)-PMO reveals a distorted structure. The intense XRD peak, assigned to the (100) plane, affirms a substantial reduction in long-range ordering when compared to the co-condensation sample.[43] The formation of a wormlike pore structure in acac(100)-PMO nanoparticles may be attributed to the reduced solubility of the acetylacetone-bridged silane, primarily due to the highly hydrophobic benzene moiety, in comparison to the other organosilica source (BTESE) in aqueous media.[43] In Fig. 1c and f, the N_2-sorption isotherms of acac-PMOs are presented. The acac(20)-PMO displays a Type IV isotherm with an H1 hysteresis loop, indicative of a uniform mesoporous structure.[31,44] Conversely, the acac(100)-PMO shows a Type IV isotherm with an H2(b)-shaped hysteresis loop, suggestive of non-uniform mesopores that are blocked for the desorption (cavitation).[45,46] Table 1 summarizes the Brunauer–Emmett–Teller surface area (S_{BET}), total pore volume at $P/P^0 = 0.95$ (V), and non-local density functional theory most prominent pore diameter (d_{NLDFT}). It is clear from the XR diffractograms, the Table 1 and the isotherms that the acac(20)-PMO, formed from 80% BTESE and only 20% acac-precursor forms the typical (expected) hexagonal structure (*P6mm*) whereas the acac(100)-PMO forms a distorted structure with uniform but unordered worm-like pores.

3.2 Luminescence properties

In the context of luminescence applications, we departed from using Eu^{3+} salts and instead employed Eu^{3+} complexes for grafting into acac(20)-PMO. Therefore, we created a composite material denoted as acac(20)-PMO@Eu_tta. The tta (thenoyltrifluoroacetonate) ligand acts as an ancillary ligand that can serve as a secondary antenna ligand. In addition, this ligand can act as a shielding agent, safeguarding the lanthanide ions from quenching by water molecules.[47]

Fig. 2a presents the excitation–emission spectra of the acac(20)-PMO under ambient conditions. The excitation spectrum displays a broad band spanning from 250 to 400 nm, with the maximum excitation wavelength at 360 nm. The emission spectrum extends from 390 to 600 nm, with the emission peak maximum at 420 nm. The luminescent properties of this hybrid material were further investigated through the grafting of $Eu(tta)_3$ complexes onto the PMO material. The combined

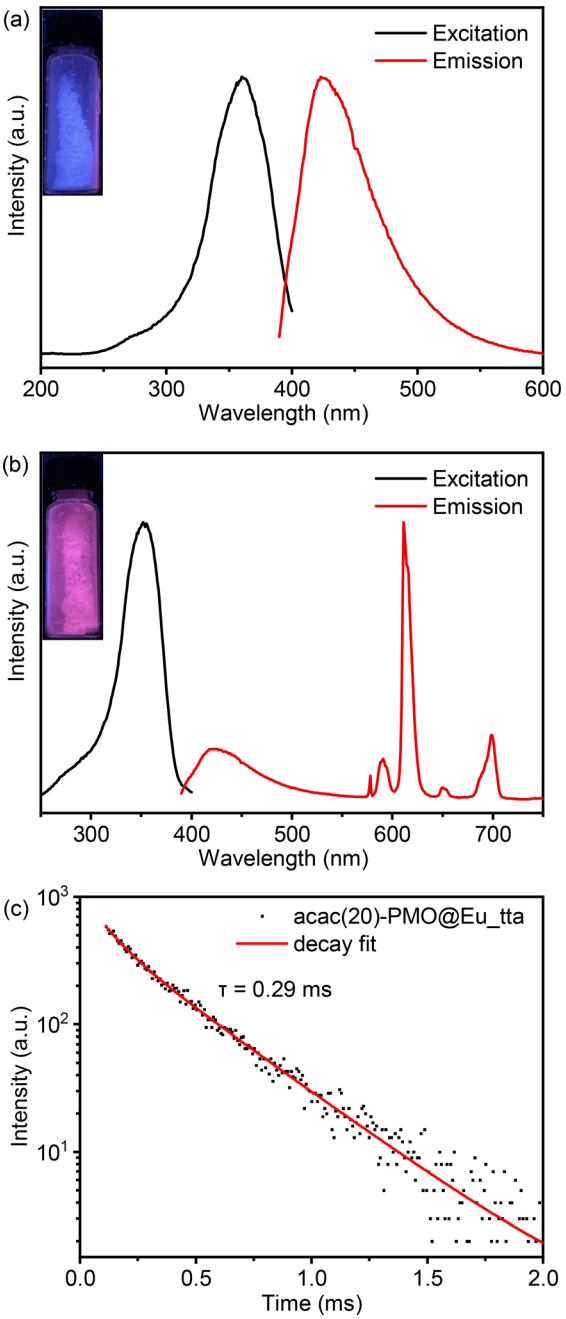

Fig. 2 (a) Combined RT excitation-emission spectrum of the acac(20)-PMO (excited at 360 nm observed at 420 nm); (b) combined RT excitation-emission spectrum of the acac(20)-PMO@Eu_tta, ex = 352 nm, em = 611 nm; (c) luminescence decay profile of as prepared acac(20)-PMO@Eu_tta, ex = 352 nm, em = 611 nm. Measurements refer to the sample in solid form.

excitation-emission spectra for acac(20)-PMO@Eu_tta are illustrated in Fig. 2b. The excitation spectrum displays a broad band spanning from 250 to 400 nm with a maximum at $\lambda_{max} = 352$ nm. This spectral feature can be attributed to transitions from the ground state $(\pi)S_0$ to the excited state $(\pi^*)S_1$ of the organic ligands. Conversely, upon excitation at the maximum of the broad band, the emission spectrum exhibits characteristics

Table 2 Assignment of acac(20)-PMO@Eu_tta emission peaks

Wavelength (nm)	Wavenumber (cm^{-1})	f–f transition
578	17 301	$^5D_0 \rightarrow {}^7F_0$
591	16 920	$^5D_0 \rightarrow {}^7F_1$
611	16 367	$^5D_0 \rightarrow {}^7F_2$
650	15 385	$^5D_0 \rightarrow {}^7F_3$
699	14 306	$^5D_0 \rightarrow {}^7F_4$

indicative of intra-$4f^6$ transitions of Eu^{3+} ions.[48] A comprehensive assignment of the emission peaks observed is provided in Table 2. When the sample is exposed to UV light (302 nm), it emits a purplish-red color, as seen in the Fig. 2b inset and the CIE diagram of Fig. S2a.† It consists of contributions from both acac(20)-PMO and Eu^{3+}. The luminescence decay time of the sample was assessed by excitation at 352 nm and detection at 611 nm. A satisfactory fit was achieved utilizing a mono-exponential decay curve (Fig. 2c).

The photophysical characteristics of acac(20)-PMO@Eu_tta are primarily ascribed to the f–f transitions of Ln^{3+} ions. The luminescence properties and the porosity of PMOs give them the ability to discern variations in their surrounding environment. This attribute allows applications in turn-off chemical sensing, achieved by modulating guest motifs through host–guest interactions.[49] To investigate the metal ion selectivity exhibited by Acac(20)-PMO@Eu_tta materials, fluorescence experiments were systematically conducted, as depicted in Fig. 3. The ion sensing performance of this material was assessed through the use of a suspension with a concentration of 1 mg mL^{-1}. In Fig. 3a, we have compiled and compared the photoluminescence spectra of interest. Most suspensions containing various metal ions (Pb^{2+}, Na^+, Al^{3+}, K^+, Mg^{2+}, Ca^{2+}, Sr^{2+}, Fe^{3+}, Hg^{2+}, Cr^{3+}, Y^{3+}, Zn^{2+}, and Cu^{2+}) exhibit the characteristic purplish-red luminescence attributed to acac(20)-pmo and Eu^{3+} transitions. However, only the presence of Cu^{2+} results in a substantial reduction in luminescence intensity, indicating a pronounced quenching effect. This observation underscores the high selectivity of acac(20)-PMO@Eu_tta for the detection and specific identification of Cu^{2+} in aqueous solutions. Notably, under UV light excitation at 302 nm, this quenching effect is visible to the naked eye (Fig. 3a inset), where the color transition from purplish-red to blue is observed. It shows the color primarily originates from acac(20)-PMO after the addition of Cu^{2+} (Fig. S2b†). It can be, in part, elucidated by the Cu(II) static quenching mechanism, which arises from the formation of non-fluorescent ground-state complexes.[50] In the PL decay time analysis shown in Fig. 3b, we also observed a decrease in the PL lifetime upon the addition of Cu^{2+}. The initial PL lifetime, recorded in the absence of Cu^{2+}, is established at 201 μs. A titration of Cu^{2+} into the system results in a measurable decrease in the PL lifetime, reaching a minimum of 175 μs. This trend confirms the quenching effect, emphasizing the selective interaction between Cu^{2+} ions and the acac(20)-PMO@Eu_tta framework. The change in decay time suggests an underlying mechanism involving energy or electron transfer, likely indicative of the formation of a charge transfer complex with Cu^{2+}, which may be attributed to both dynamic quenching and the paramagnetic nature of the Cu^{2+} ions.[51,52] Luminescence titration experiments were conducted to investigate the luminescent response of acac(20)-PMO@Eu_tta in the presence of Cu^{2+} ions. With an increasing concentration of Cu^{2+} ions, there was a marked reduction in the emission intensity of acac(20)-PMO@Eu_tta, as depicted in Fig. 3c. This effect resulted in the complete quenching of fluorescence emission in the Eu^{3+} hybrid suspension when the Cu^{2+} concentration reached 30 μM (Fig. S3†). To quantitatively assess this luminescence quenching effect, we employed the Stern–Volmer (S–V) equation. The Stern–Volmer quenching constant (K_{SV}) was calculated as a measure of the quenching efficiency and enabling a precise characterization of the interaction between acac(20)-PMO@Eu_tta and Cu^{2+} ions:

$$\frac{I_0}{I} = K_{SV}c + 1 \quad (1)$$

where I_0 and I are the luminescence intensities of acac(20)-PMO@Eu_tta suspension before and after the addition of the Cu^{2+} ion, respectively, and c is the molar concentration of Cu^{2+}.[27,53] A linear relation ($R^2 = 0.996$) was achieved in the concentration range of 0 to 2.5 μM (Fig. 3d). The calculated K_{sv} value is 180 198 M^{-1}. The limit of detection (LOD) was calculated to be 108 nM (26 ppb) according to the method used by Armbruster *et al.*, assuming that

$$\mathrm{LOD} = 3\sigma/K_{SV} \quad (2)$$

where σ represents the standard deviation of the response, which can be determined by assessing the standard deviation of measurements from the blank sample.[54–56] The calculated value was significantly lower than the permissible level of Cu^{2+} in drinking water, which is set at 1.3 ppm (6.9 μM) by the Environmental Protection Agency (EPA).[57] Selectivity plays a pivotal role in assessing the effectiveness of a sensing material for the detection of specific analytes in real-world applications, as it determines the material's ability to distinguish the target analyte from other environmental components.[58] The relative PL intensity of the probe was assessed following the introduction of various common metal ions, each at the same concentration. These metal ions included Pb^{2+}, Na^+, Al^{3+}, K^+, Mg^{2+}, Ca^{2+}, Sr^{2+}, Fe^{3+}, Hg^{2+}, Cr^{3+}, Y^{3+}, Zn^{2+}, and Cu^{2+}, as depicted in Fig. 3e. Only upon the addition of Cu^{2+} ions to metal ion-enriched PMO dispersions, a significant quenching of the photoluminescence (PL) intensity was observed. This effect underscores the acac(20)-PMO@Eu_tta's high selectivity for Cu^{2+}, distinguishing it from a variety of other metal ions. Notably, the method's selectivity was evident in distinguishing Cu^{2+} ions from Hg^{2+} and Pb^{2+}, which are common competitors often encountered in real-world field samples. Furthermore, in comparison to prior Cu^{2+} sensing methods based on nanoparticle fluorometric sensors in aqueous system, the proposed approach exhibits a comparable linear range and selectivity, and sensitivity, as summarized in Table S1.†[59,60] To date, only a limited number of copper sensors based on LnPMOs have been reported as turn-on fluorescence chemical sensors.[29,31]

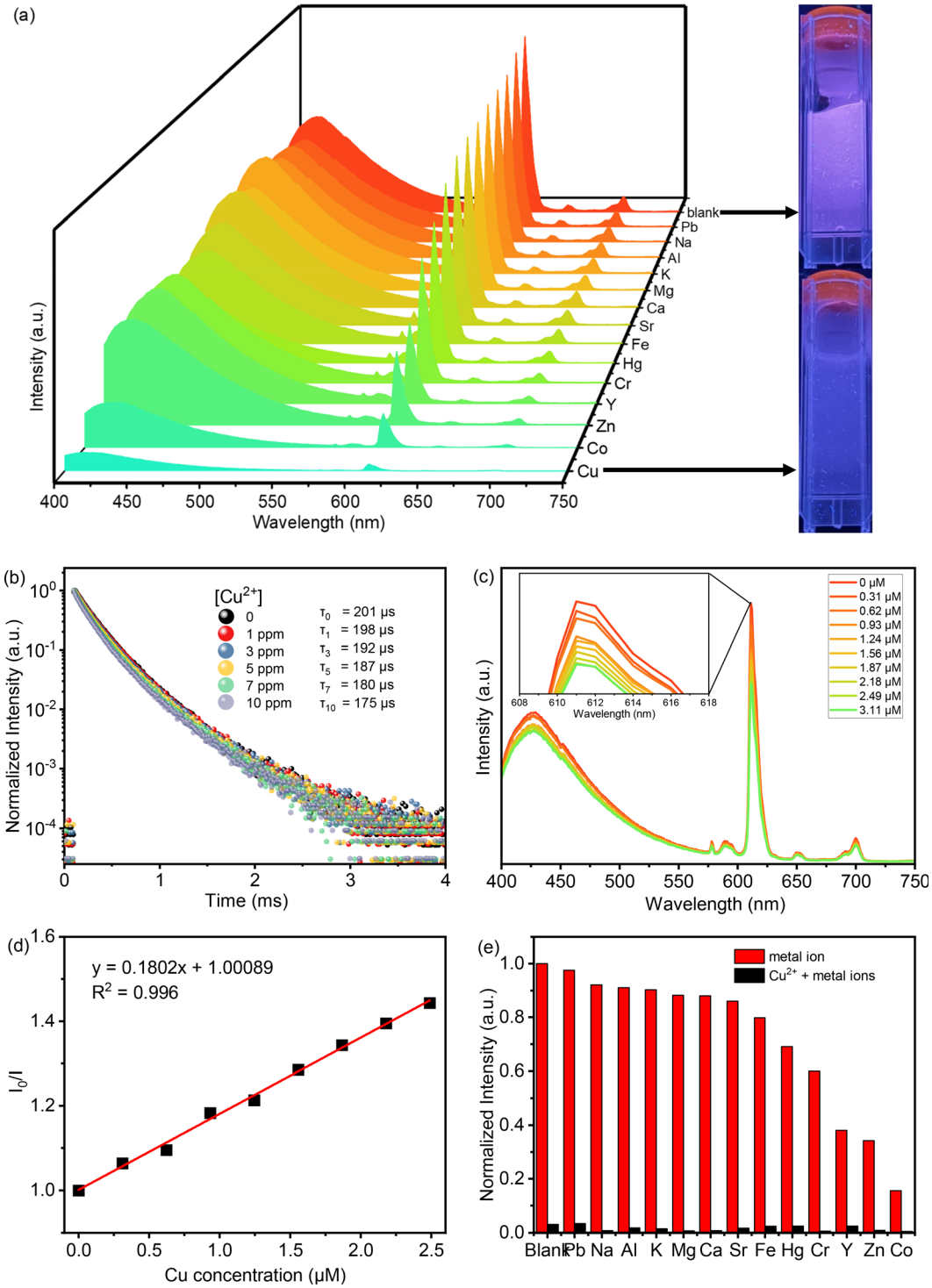

Fig. 3 (a) Emission spectra of the colloidal suspensions of acac(20)-PMO@Eu_tta in the presence of different metal ions (1000 ppm) (Pb^{2+}, Na^{+}, Al^{3+}, K^{+}, Mg^{2+}, Ca^{2+}, Sr^{2+}, Fe^{3+}, Hg^{2+}, Cr^{3+}, Y^{3+}, Zn^{2+}, and Cu^{2+}) when excited at 343 nm; (b) luminescence decay profile of colloidal suspensions of acac(20)-PMO@Eu_tta before and after the addition of Cu^{2+} ions. (c) Luminescence spectra of acac(20)-PMO@Eu_tta under different concentrations of Cu^{2+} aqueous solutions; (d) plot of the Stern–Volmer curve between the luminescence intensity and Cu^{2+} concentration in an aqueous solution; (e) comparison of the luminescence intensities (611 nm) of acac(20)-PMO@Eu_tta with varied ions (1000 ppm) (Pb^{2+}, Na^{+}, Al^{3+}, K^{+}, Mg^{2+}, Ca^{2+}, Sr^{2+}, Fe^{3+}, Hg^{2+}, Cr^{3+}, Y^{3+}, and Zn^{2+}) before and after treated by Cu^{2+}.

3.3Catalytic properties

The acac(100)-PMO was utilized as a heterogeneous catalysis by anchoring $VO(acac)_2$ onto the material, resulting in a catalyst containing 0.59 mmol V g^{-1} (cat). The surface elemental composition of acac(100)-PMO and acac(100)-PMO@VO_acac was analyzed using XPS. Fig. 4a and d illustrate the presence of elements such as V, C, O, and Si on the surfaces of these nanocomposites. In Fig. 4b and e, the C 1s region reveals the

presence of multiple chemical states of carbon. Four distinct peaks were discerned and attributed to C–Si(282.6 eV), C–C and C–H (284.8 eV), C–O (286.9 eV), and C=O species (289.8 eV).[61] The increasing peak of C=O can be attributed to the grafting of $VO(acac)_2$. In the XPS O 1s spectra, two distinct peaks were observed at 531.9 and 532.9 eV. These peaks can be attributed to the presence of C=O and –C–OH groups, likely arising from the tautomerization of the acac group in both its keto and enol forms, as illustrated in Fig. 4c and f. The high-resolution XPS spectrum of V 2p can be deconvoluted into two primary doublet peaks, as depicted in Fig. S5.† In this detailed spectrum, the doublet peaks at 515.3 eV and 522.2 eV correspond to V $2p_{3/2}$ and V $2p_{1/2}$, respectively.[62] This observation suggests the presence of V(IV) in the acac(100)-PMO@VO_acac.

Upon completing the material characterization, the catalytic performance of the acac(100)-PMO@VO_acac material was tested for the model Mannich-type reaction, as shown in Table 3. During a typical catalytic test, predetermined quantities of 2-naphthol and *N*-methylmorpholine *N*-oxide (NMO), along with the catalyst were combined. The mixture was then refluxed in anhydrous DCM within a 10 mL Schlenk tube under an inert atmosphere. At specific time intervals, the catalyst was separated, and the filtrate was evaporated until dryness, resulting in the formation of the pure Mannich base with a quantitative yield.[17] The confirmation of product formation was achieved through ^{1}H NMR spectroscopy.

Initially, the Mannich type reaction between 2-naphthol (**1a**) and 4-methylmorpholine *N*-oxide (NMO) (**2a**) was conducted in the absence of a catalyst at 40 °C. After 12 hours of reaction, no substrate conversion occurred, highlighting the necessity of the presence of a catalyst (Table 3, entry 2). Subsequently, we investigated the catalytic activity of $VO(acac)_2$ for this model reaction. This complex exhibited a yield of 92% after 12 hours of reaction. However, it is hard to recycle this homogeneous catalyst.[17,18,20] For the heterogeneous acac(100)-PMO@VO_acac catalyst, a 16% yield of the major product, 1-(morpholinomethyl)naphthalen-2-ol (**3a**), was obtained within 60 minutes.[17,63] An increase in the yield from 40% to 98% was obtained upon extending the reaction time from 6 to 12 hours. Moreover, we conducted the reaction multiple times with varying equivalents of NMO. When employing 1, 1.5, 2, or 3 equivalents of NMO under the optimized reaction conditions, we observed yields of 70%, 96% and 98% of **3a**, respectively. The highest yield of 92% for **3a** was achieved using 3 equivalents of NMO.

The recyclability and structural stability of acac(100)-PMO@VO_acac material were studied during the preparation of 1(morpholinomethyl)naphthalen-2-ol under optimized

Table 3 Role of different reaction conditions for preliminary Mannich-type reaction[a]

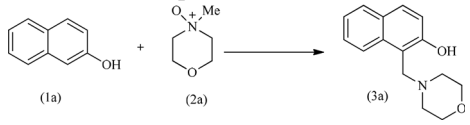

Entry	Catalyst	**1a : 2a**	Time (h)	Yield[b] (%)
1	—	1 : 2	12	—
2	$VO(acac)_2$[c]	1 : 3	12	92
3	acac(100)-PMO	1 : 3	12	—
4	acac(100)-PMO@VO_acac	1 : 3	12	98
5	acac(100)-PMO@VO_acac	1 : 2	12	98
6	acac(100)-PMO@VO_acac	1 : 1.5	12	96
7	acac(100)-PMO@VO_acac	1 : 1	12	70
8	acac(100)-PMO@VO_acac	1 : 2	1	16
9	acac(100)-PMO@VO_acac	1 : 2	6	40
10	acac(100)-PMO@VO_acac	1 : 2	24	98

[a] Reaction conditions: 2-naphthol (1 mmol), NMO, DCM (2 mL) and catalyst (15 mg). [b] Yield was calculated from ^{1}H NMR analysis using mesitylene as internal standard. [c] 10 mol%.

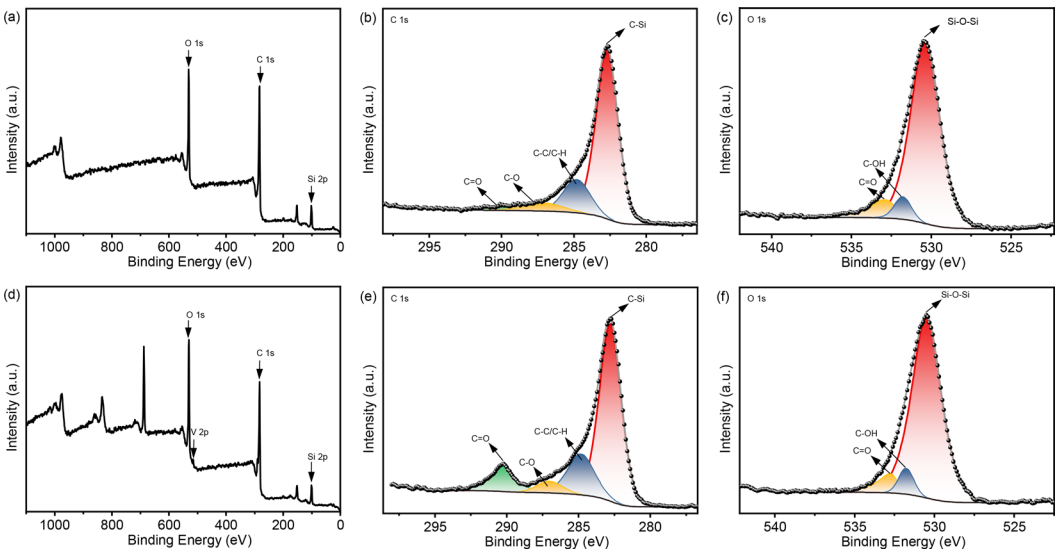

Fig. 4 XPS spectra of (a) acac(100)-PMO, in the regions of (b) C 1s and (c) O 1s; and (d) acac(100)-PMO@VO_acac, in the regions of (e) C 1s and (f) O 1s.

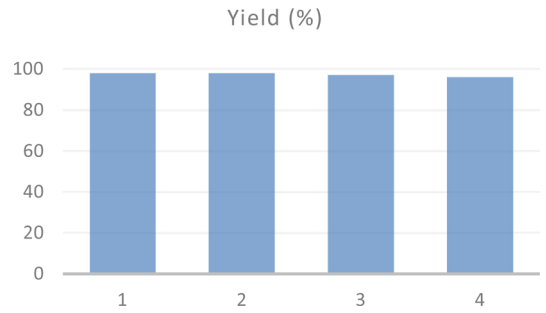

Fig. 5 Recycling test of acac(100)-PMO@VO_acac catalyst for Mannich-type reaction.

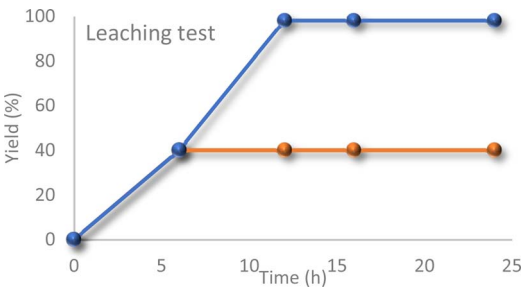

Fig. 6 Reaction profile with or without the catalyst (after separating the catalyst from the reaction mixture *via* hot-filtration technique).

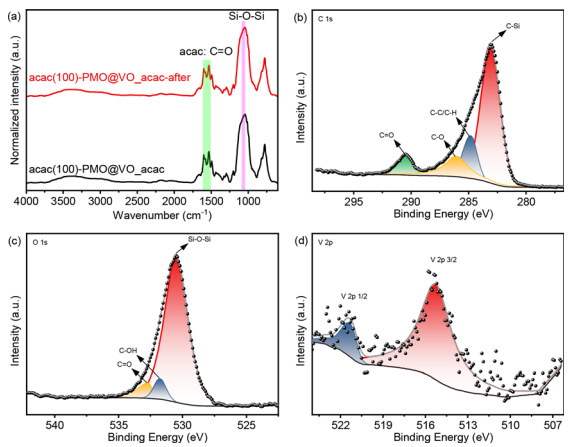

Fig. 7 (a) DRIFT spectra of acac(100)-PMO@VO_acac before and after Mannich-type reaction; (b) deconvoluted XPS C 1s spectra, (c) O 1s spectra and (d) vanadium in the V 2p region of the recycled acac(100)-PMO@VO_acac.

reaction conditions. After completing the reaction, the recyclability test was conducted using the recovered catalyst. The catalyst was thoroughly washed with dichloromethane and dried under vacuum at 120 °C before being utilized in the subsequent catalytic reaction. The catalyst demonstrated consistent activity, with no significant decrease up to the four tested cycles (Fig. 5).

Furthermore, a hot filtration test was performed to assess the potential leaching of vanadium ions from the support. The catalyst was removed from the reaction mixture after 6 hours, and the reaction was allowed to continue for an additional 18 hours (Fig. 6). No further progress was observed in the reaction, indicating the absence of leaching.

To examine the physio-chemical properties of the catalyst, FT-IR and XPS analyses were conducted, as depicted in Fig. 7. The recovered catalyst exhibited all the characteristic peaks, similar to the fresh catalyst. Additionally, the XPS analysis of the recycled catalyst (Fig. 7b–d) displayed the same specific peaks as the fresh catalyst. These results confirm that the chemical structure of the catalyst was preserved during the recycling process.

The catalytic reactivity of the acac(100)-PMO@VO_acac catalyst was evaluated using a diverse range of substrates, including 2-naphthol, 1-naphthol, and phenol derivatives, under the optimized reaction conditions (Table 4). Substantial catalytic conversion was achieved for nearly all the substrates, regardless of whether they had electron-donating or electron-withdrawing substituents on the aromatic ring.

In Scheme S1,† a plausible pathway for the preparation of the Mannich base was proposed, following similar steps as previously reported by Uang *et al.*[17,63–65] Initially, the active V=O groups of the catalyst formed complexes with 4-methylmorpholine *N*-oxide, leading to the formation of a six-membered structure (A). An intramolecular elimination process *via* this transition structure resulted in the formation of an iminium ion B structure. Second, the [V(OH)(O^-)] species played a crucial role in abstracting an acidic proton from 2-naphthol, generating a negatively charged oxygen species. This species further creates an acidic carbon center. A target Mannich base formed through a reaction of this acidic carbon center with iminium ions. Finally, the elimination of water molecules from $V(OH)_2$ regenerated the catalyst, completing the catalytic cycle.

The catalytic performance of acac(100)-PMO@VO_acac was compared to its homogeneous counterpart, $VO(acac)_2$, as well as acac-based covalent triazine frameworks (CTFs) and covalent organic frameworks (COFs) in Table S2.†[17,63,64,66] It is evident from Table S2† that the acac(100)-PMO@VO_acac catalyst resulted in the targeted product with a high yield and conversion rate. When compared with $VO(acac)_2$, it exhibited a higher yield (98%) and turnover number (TON) of 111, which is 12 times greater than the TON achieved by the homogeneous catalyst. Moreover, we evaluated the catalytic activity of acac(100)-PMO@VO_acac in comparison to acac-based COFs, such as vanadium-docked COFs (VO-TAPT-2,3-DHTA COF, VO-PyTTA-2,3-DHTA COF). In these cases, the catalysts resulted in the targeted product with yield of 98% and 96%, along with TON values of 29 and 36, respectively. This combination of high conversion and TON suggests potential for acac(100)-PMO@VO_acac as a heterogeneous catalyst. These findings substantiate the promising future of acac-PMO materials as versatile supports for the development of advanced heterogeneous catalysts.

Table 4 Mannich-type reaction with differently substituted substrates catalyzed by acac(100)-PMO@VO_acac.[a]

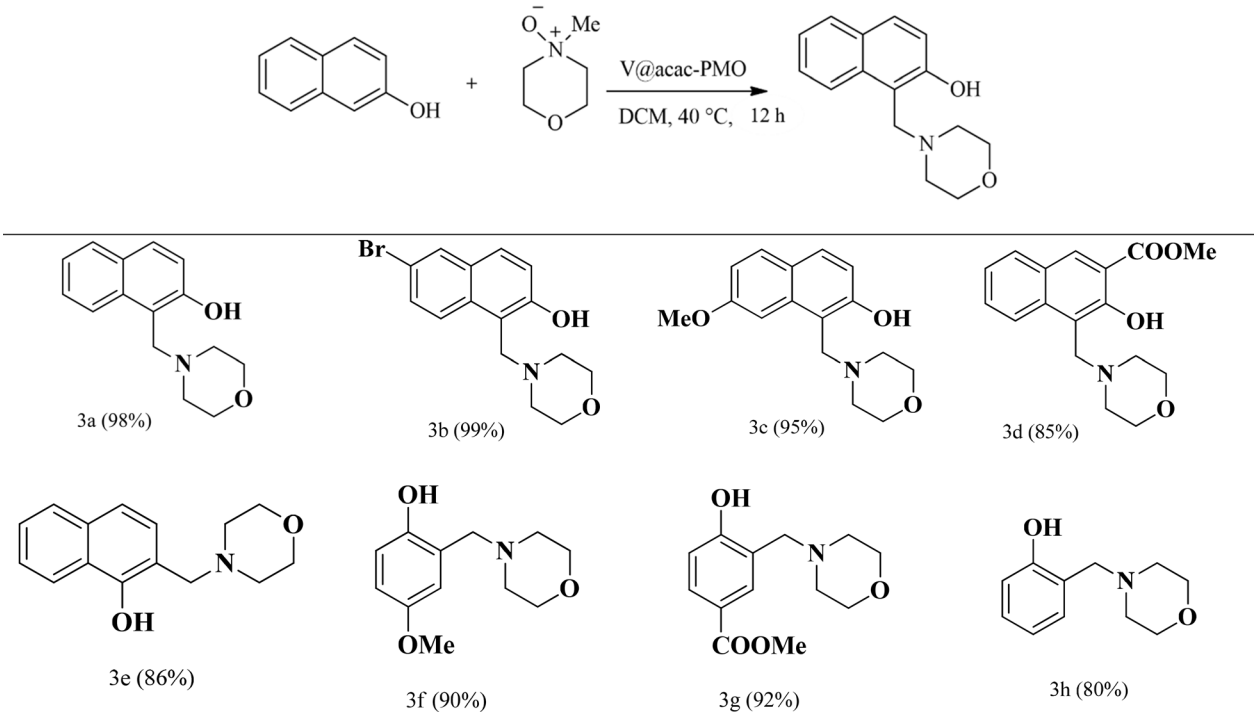

[a] Yields are calculated from ^{1}H NMR using mesitylene as an internal standard.

4 Conclusions

This study introduces a novel PMOs with embedded acetylacetone (acac) groups, showcasing its dual utility in catalysis and sensing. The acac(20)-PMO grafted with Eu(tta)$_3$ demonstrates effectiveness as a luminescent sensor towards aqueous Cu^{2+} ions, achieving a LOD of 108 nM. In addition, a heterogeneous catalyst (acac(100)-PMO@VO_acac) was prepared by anchoring VO(acac)$_2$ on pristine acac-PMO that showed high reactivity in a modified Mannich reaction with a turnover number (TON) of 111 and a wide substrate scope. Furthermore, the embedded acac functionality's capacity to tether "hard" metal ions suggests potential applications in sensing, catalysis, and water purification. These findings underscore the versatility of acac-PMOs and open new avenues for their application in environmental and industrial contexts.

Data availability

The data supporting this article have been included as part of the ESI.†

Conflicts of interest

There are no conflicts to declare.

Acknowledgements

C. H. L. gratefully acknowledges the financial support from the China Scholarship Council (201908110280). P. V. D. V. acknowledges Hercules Project AUGE/17/07 for the UV VIS DRS spectrometer and UGent BASBOF BOF20/BAS/015 for the powder X-Ray Diffractometer. The authors thank Prof. Rik Van Deun for access to the spectrofluorometer in his lab. The authors thank Katrien Haustraete for STEM-EDX measurements, within the UGent TEM core facility. The authors thank Dr Karen Leus for the XPS measurements.

References

1 S. S. Park, M. S. Moorthy and C. S. Ha, *NPG Asia Mater.*, 2014, **6**, e96.
2 T. Asefa, M. J. MacLachlan, N. Coombs and G. A. Ozin, *Nature*, 1999, **402**, 867–871.
3 B. J. Melde, B. T. Holland, C. F. Blanford and A. Stein, *Chem. Mater.*, 1999, **11**, 3302–3308.
4 S. Inagaki, S. Guan, Y. Fukushima, T. Ohsuna and O. Terasaki, *J. Am. Chem. Soc.*, 1999, **121**, 9611–9614.
5 C. T. Kresge, M. E. Leonowicz, W. J. Roth, J. C. Vartuli and J. S. Beck, *Nature*, 1992, **359**, 710–712.
6 D. Zhao, J. Feng, Q. Huo, N. Melosh, G. H. Fredrickson, B. F. Chmelka and G. D. Stucky, *Science*, 1998, **279**, 548–552.
7 M. Ferré, R. Pleixats, M. Wong Chi Man and X. Cattoën, *Green Chem.*, 2016, **18**, 881–922.
8 P. Van der Voort, D. Esquivel, E. De Canck, F. Goethals, I. Van Driessche and F. J. Romero-Salguero, *Chem. Soc. Rev.*, 2013, **42**, 3913–3955.
9 Y. Wei, X. Li, R. Zhang, Y. Liu, W. Wang, Y. Ling, A. M. El-Toni and D. Zhao, *Sci. Rep.*, 2016, **6**, 20769.

10 A. M. Kaczmarek, S. Abednatanzi, D. Esquivel, C. Krishnaraj, H. S. Jena, G. B. Wang, K. Leus, R. Van Deun, F. J. Romero-Salguero and P. Van der Voort, *Microporous Mesoporous Mater.*, 2020, **291**, 109687.
11 A. A. Gismatulin, V. A. Gritsenko, D. S. Seregin, K. A. Vorotilov and M. R. Baklanov, *Appl. Phys. Lett.*, 2019, **115**, 082904.
12 X. Feng, F. Li, L. Zhang, W. Liu, X. Wang, R. Zhu, Z. A. Qiao, B. Yu and X. Yu, *Acta Biomater.*, 2022, **143**, 392–405.
13 A. M. Kaczmarek and P. Van der Voort, *J. Mater. Chem. C*, 2019, **7**, 8109–8119.
14 M. A. Bennett, M. J. Byrnes and I. Kovacik, *J. Organomet. Chem.*, 2004, **689**, 4463–4474.
15 P. Muraoka, D. Byun and J. I. Zink, *Coord. Chem. Rev.*, 2000, **208**, 193–211.
16 W. H. Wang, T. L. Yung, S. S. Cheng, F. Chen, J. B. Liu, C. H. Leung and D. L. Ma, *Sens. Actuators, B*, 2020, **321**, 128486.
17 H. S. Jena, C. Krishnaraj, G. B. Wang, K. Leus, J. Schmidt, N. Chaoui and P. Van der Voort, *Chem. Mater.*, 2018, **30**, 4102–4111.
18 A. R. Hajipour and G. Azizi, *Green Chem.*, 2013, **15**, 1030–1034.
19 A. Hajipour and G. Azizi, *Appl. Organomet. Chem.*, 2015, **29**, 247–253.
20 P. Borah, X. Ma, K. T. Nguyen and Y. Zhao, *Angew. Chem., Int. Ed.*, 2012, **51**, 7756–7761.
21 B. B. Lai, Z. P. Huang, Z. F. Jia, R. X. Bai and Y. L. Gu, *Catal. Sci. Technol.*, 2016, **6**, 1810–1820.
22 C. Pereira, A. R. Silva, A. P. Carvalho, J. Pires and C. Freire, *J. Mol. Catal. A: Chem.*, 2008, **283**, 5–14.
23 S. V. Eliseeva and J. C. Bunzli, *Chem. Soc. Rev.*, 2010, **39**, 189–227.
24 C. H. Liu, A. M. Kaczmarek, H. S. Jena, Z. T. Yang, D. Poelman and P. van der Voort, *J. Mater. Chem. C*, 2023, **11**, 5634–5645.
25 Y. Liu, Q.-L. Shi and J.-L. Yuan, *Chin. Chem. Lett.*, 2015, **26**, 1485–1489.
26 H. Li, Y. Li, Z. Zhang, X. Pang and X. Yu, *Mater. Des.*, 2019, **172**, 107712.
27 A. M. Kaczmarek and P. Van Der Voort, *J. Mater. Chem. C*, 2019, **7**, 8109–8119.
28 A. M. Kaczmarek, S. Abednatanzi, D. Esquivel, C. Krishnaraj, H. S. Jena, G. Wang, K. Leus, R. Van Deun, F. J. Romero-Salguero and P. Van Der Voort, *Microporous Mesoporous Mater.*, 2020, **291**, 109687–109688.
29 W. Liu, A. M. Kaczmarek, H. Rijckaert, P. Van Der Voort and R. Van Deun, *Dalton Trans.*, 2021, **50**, 11061–11070.
30 W. Liu, A. M. Kaczmarek, P. Van Der Voort and R. Van Deun, *Dalton Trans.*, 2022, **51**, 11467–11475.
31 H. Li, Y. J. Li, Z. Zhang, X. L. Pang and X. D. Yu, *Mater. Des.*, 2019, **172**, 107712.
32 Y. Su, D. Zhang, P. Jia, W. Gao, Y. Li, J. He, C. Wang, X. Zheng, Q. Yang and C. Yang, *Eur. Polym. J.*, 2019, **112**, 461–465.
33 R. R. Ma, Z. W. Chen, S. N. Wang, Q. X. Yao, Y. W. Li, J. Lu, D. C. Li and J. M. Dou, *J. Solid State Chem.*, 2017, **252**, 142–151.
34 N. Ding, D. L. Zhou, G. C. Pan, W. Xu, X. Chen, D. Y. Li, X. H. Zhang, J. Y. Zhu, Y. A. Ji and H. W. Song, *ACS Sustainable Chem. Eng.*, 2019, **7**, 8397–8404.
35 Z. G. Lin, F. Q. Song, H. Wang, X. Q. Song, X. X. Yu and W. S. Liu, *Dalton Trans.*, 2021, **50**, 1874–1886.
36 N. Brun, B. Julian-Lopez, P. Hesemann, G. Laurent, H. Deleuze, C. Sanchez, M. F. Achard and R. Backov, *Chem. Mater.*, 2008, **20**, 7117–7129.
37 K. Binnemans, P. Lenaerts, K. Driesen and C. Görller-Walrand, *J. Mater. Chem.*, 2004, **14**, 191–195.
38 L. Carlucci, G. Ciani, S. Maggini, D. M. Proserpio and M. Visconti, *Chem.–Eur. J.*, 2010, **16**, 12328–12341.
39 Z. Zhang, H. Chang, Y. F. Kang, X. P. Li, H. Jiang, B. L. Xue, Y. Y. Wang, X. Q. Lü and X. J. Zhu, *Sens. Actuators, B*, 2019, **282**, 999–1007.
40 L. Bourda, H. S. Jena, R. Van Deun, A. M. Kaczmarek and P. Van der Voort, *J. Mater. Chem. A*, 2019, **7**, 14060–14069.
41 A. M. Kaczmarek, Y. Maegawa, A. Abalymov, A. G. Skirtach, S. Inagaki and P. Van Der Voort, *ACS Appl. Mater. Interfaces*, 2020, **12**, 13540–13550.
42 G. Chandrasekar, K. S. You, J. W. Ahn and W. S. Ahn, *Microporous Mesoporous Mater.*, 2008, **111**, 455–462.
43 B. Guan, Y. Cui, Z. Ren, Z. A. Qiao, L. Wang, Y. Liu and Q. Huo, *Nanoscale*, 2012, **4**, 6588–6596.
44 E. Valiey and M. G. Dekamin, *Nanoscale Adv.*, 2022, **4**, 294–308.
45 P. Van Der Voort, K. Leus and E. De Canck, *Introduction to Porous Materials*, John Wiley & Sons, 2019.
46 M. Thommes, K. Kaneko, A. V. Neimark, J. P. Olivier, F. Rodriguez-Reinoso, J. Rouquerol and K. S. Sing, *Pure Appl. Chem.*, 2015, **87**, 1051–1069.
47 A. M. Kaczmarek, Y. Y. Liu, M. K. Kaczmarek, H. Liu, F. Artizzu, L. D. Carlos and P. Van Der Voort, *Angew. Chem.*, 2020, **132**, 1948–1956.
48 X. Guo, X. Wang, H. Zhang, L. Fu, H. Guo, J. Yu, L. D. Carlos and K. Yang, *Microporous Mesoporous Mater.*, 2008, **116**, 28–35.
49 J. Lin, Q. Cheng, J. Zhou, X. Lin, R. C. K. Reddy, T. Yang and G. Zhang, *J. Solid State Chem.*, 2019, **270**, 339–345.
50 N. Ding, D. L. Zhou, G. C. Pan, W. Xu, X. Chen, D. Y. Li, X. H. Zhang, J. Y. Zhu, Y. A. Ji and H. W. Song, *ACS Sustainable Chem. Eng.*, 2019, **7**, 8397–8404.
51 T. Kohlmann and M. Goez, *Phys. Chem. Chem. Phys.*, 2019, **21**, 10075–10085.
52 L. Li, S. Shen, R. Lin, Y. Bai and H. Liu, *Chem. Commun.*, 2017, **53**, 9986–9989.
53 G. Ji, J. Liu, X. Gao, W. Sun, J. Wang, S. Zhao and Z. Liu, *J. Mater. Chem. A*, 2017, **5**, 10200–10205.
54 D. A. Armbruster and T. Pry, *Clin. Biochem. Rev.*, 2008, **29**, S49.
55 M. E. Zorn, R. D. Gibbons and W. C. Sonzogni, *Anal. Chem.*, 1997, **69**, 3069–3075.
56 E. Mohamed Ali, Y. Zheng, H.-h. Yu and J. Y. Ying, *Anal. Chem.*, 2007, **79**, 9452–9458.

57 U. Latief, S. Ul Islam, Z. Khan and M. S. Khan, *J. Alloys Compd.*, 2022, **910**, 164889.
58 H. Li, Y. Li, Z. Zhang, X. Pang and X. Yu, *Mater. Des.*, 2019, **172**, 107712.
59 T. Chopra, S. Sasan, L. Devi, R. Parkesh and K. K. Kapoor, *Coord. Chem. Rev.*, 2022, **470**, 214704.
60 X. G. Liu, D. L. Huang, C. Lai, G. M. Zeng, L. Qin, H. Wang, H. Yi, B. S. Li, S. Y. Liu, M. M. Zhang, R. Deng, Y. K. Fu, L. Li, W. J. Xue and S. Chen, *Chem. Soc. Rev.*, 2019, **48**, 5266–5302.
61 Y. Peng, N. Pan, D. Wang, J. Yang, Z. Guo and W. Yuan, *J. Mater. Sci.*, 2018, **53**, 12432–12440.
62 P. Borah, X. Ma, K. T. Nguyen and Y. Zhao, *Angew Chem. Int. Ed. Engl.*, 2012, **51**, 7756–7761.
63 H. Vardhan, L. X. Hou, E. Yee, A. Nafady, M. A. Al-Abdrabalnabi, A. M. Al-Enizi, Y. X. Pan, Z. Y. Yang and S. Q. Ma, *ACS Sustainable Chem. Eng.*, 2019, **7**, 4878–4888.
64 D. R. Hwang and B. J. Uang, *Org. Lett.*, 2002, **4**, 463–466.
65 X. Chen, N. Huang, J. Gao, H. Xu, F. Xu and D. Jiang, *Chem. Commun.*, 2014, **50**, 6161–6163.
66 P. P. Reddy, C. Y. Chu, D. R. Hwang, S. K. Wang and B. J. Uang, *Coord. Chem. Rev.*, 2003, **237**, 257–269.